LASER & PHOTONICS REVIEWS
www.lpr-journal.org

Highly Efficient Transfer of Quantum State and Robust Generation of Entanglement State Around Exceptional Lines

Zan Tang, Tian Chen, and Xiangdong Zhang**

Exceptional points (EPs) are non-Hermitian degeneracies or branch points where eigenvalues and their corresponding eigenvectors coalesce. Due to the complex non-trivial topology of Riemann surfaces associated with non-Hermitian Hamiltonians, the dynamical encirclement or proximity of EPs in parameter space has been shown to lead to topological mode conversions and some novel physical phenomena. In fact, degeneracies can also form continuous line geometries, which are called exceptional lines (ELs). The problem is whether the state transfer around the ELs can show different characteristics from the EPs, which is less explored. Here, novel properties of quantum state transfer around the ELs based on a quantum walk platform are explored. It is found that the evolutionary state around the ELs is independent of the initial state and evolution direction, and the transfer of quantum state is more efficient than the case around the EPs. Furthermore, based on such a property, an entangled state generation insensitive to the incident state is realized experimentally. The work opens up a new way for the application of non-Hermitian physics in the field of quantum information.

1. Introduction

The study of non-Hermitian systems has attracted more and more attention, because physical properties in many real systems should be described by non-Hermitian Hamiltonians.[1–7] The systems driven by non-Hermitian Hamiltonians exhibit exotic properties compared with those governed by Hermitian Hamiltonians, which have been demonstrated in various systems.[8–26] One of the distinct features is that spectral degeneracy induced by parity-time (PT)-symmetry[3] can lead to the existence of exceptional points (EPs), at which both the eigenvalues and the corresponding eigenvectors coalesce.[4,5] Around or near the EPs, the abrupt nature of the phase transitions has been shown to lead to many intriguing phenomena, such as topological mode and energy transfers,[27–41] laser mode selectivity,[42–44] EP-enhanced mode splitting,[45–60] loss-induced transparency,[61,62] unidirectional invisibility[63] and many others.[64–67] Additionally, the coherent flow induced by exceptional points has been experimentally demonstrated in optics, [68] and quantum Liouvillian exception points in open systems have been studied.[69–71] In contrast to the isolated EPs, the eigenvector and eigenenergy of the system degenerate in many positions, these degenerate points are connected, and their tracks form lines, which are called exceptional lines (ELs). It is natural to ask whether the state transfer around the ELs, especially for quantum states and generation of entanglement states, can show different characteristics from the EPs. Such a problem has never been studied because of the complexity of the problem itself.

On the other hand, highly efficient transfer of quantum states and robust generation of entanglement states are crucial for applications in quantum information.[72–74] However, it is hard to achieve at present because of quantum decoherence and disorder. Moreover, some recent works on quantum walk (QW) have been implemented on optical[75] and superconducting[76] platforms, demonstrating the powerful ability to simulate quantum systems. In this work, we demonstrate both theoretically and experimentally that highly efficient transfer of quantum states and robust generation of entanglement states can be realized by constructing the system with the ELs. To show it, the QW platform has been constructed. Not only the relevant theories have been developed, but also the experiments have been performed. It is shown that the evolutionary state around the ELs is independent of the initial state and evolution direction, and the transfer of quantum state is more efficient than the case around the EPs. Furthermore, based on such a property, the generation of an entangled state insensitive to the incident state is realized experimentally. All of these phenomena are attributed to the topological properties of the Riemann surface in our constructed QW, which leads to high state transfer efficiency compared with the other schemes without ELs or EPs, especially considering the external influence.

Z. Tang, T. Chen, X. Zhang
Key Laboratory of Advanced Optoelectronic Quantum Architecture and Measurements of Ministry of Education
Beijing Key Laboratory of Nanophotonics & Ultrafine Optoelectronic Systems
School of Physics
Beijing Institute of Technology
Beijing 100081, China
E-mail: chentian@bit.edu.cn; zhangxd@bit.edu.cn

The ORCID identification number(s) for the author(s) of this article can be found under https://doi.org/10.1002/lpor.202300794

DOI: 10.1002/lpor.202300794

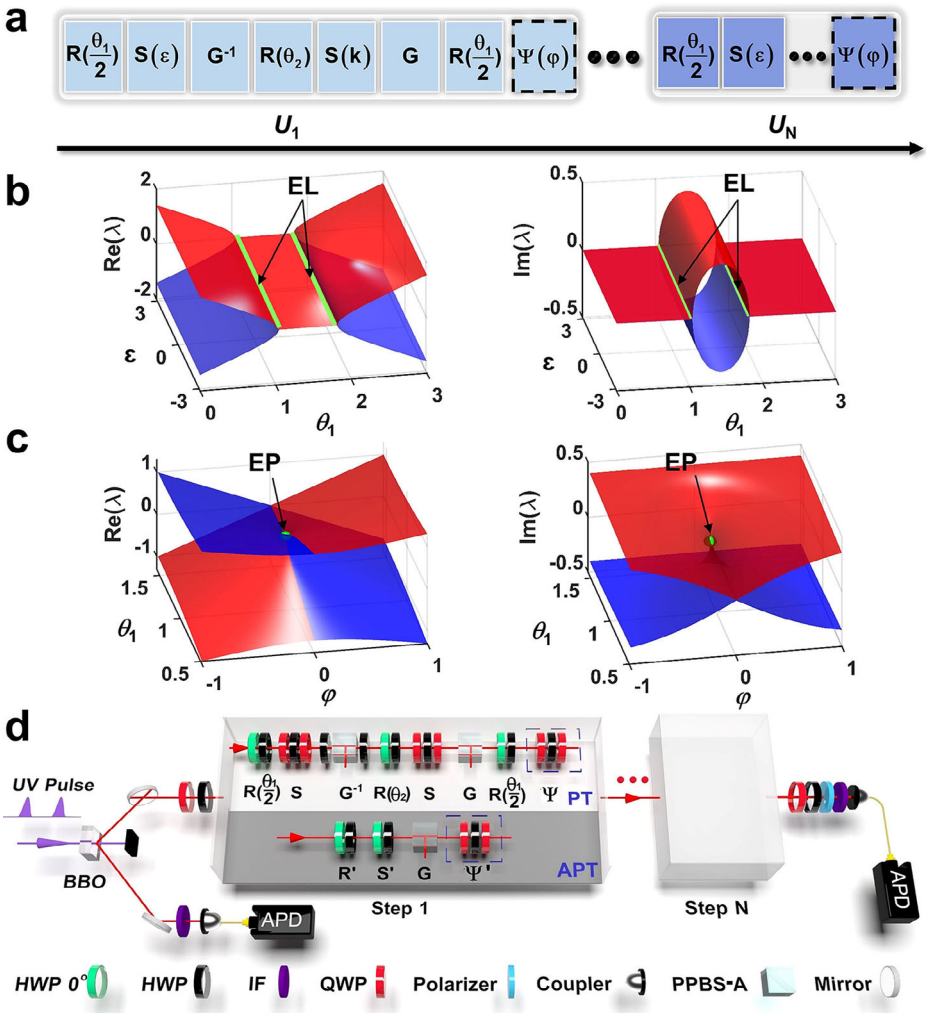

Figure 1. Dynamic evolution of quantum states based on quantum walks (QWs). a) The parity-time (PT) symmetric QWs. b,c) energy spectrum with exceptional lines (ELs) and an exceptional point (EP), respectively. d) The experimental setup for quantum state transfer. The white boxes repeat operators at step 1. White and gray areas denote PT and anti-parity-time (APT) symmetric QWs, respectively.

2. Dynamical Loop Evolution of Quantum States Based on QWs

2.1. Constructions of QWs with Exceptional Points or Exceptional Lines

In previous studies,[27–36] the dynamic encircling of the exceptional point was described using Hamiltonian operators. In the following, we provide another way to describe such a problem, that is, utilize non-Hermitian evolution operators based on QWs. As illustrated in **Figure 1**a, a non-Hermitian QW system containing N steps is constructed to control the evolution of quantum states, where the evolution of step 1 (N) is described by the operator U_1 (U_N). The time-evolution operator of the QWs, which fits in the symmetry time frame of the momentum representation, consists of multiple operations. For example, U_1 is expressed as:

$$U_1 = R\left(\frac{\theta_1}{2}\right) \mathrm{GSR}\left(\theta_2\right) G^{-1} \mathrm{SR}\left(\frac{\theta_1}{2}\right) \tag{1}$$

where $R(\theta) = \begin{pmatrix} \cos(\theta) & -\sin(\theta) \\ \sin(\theta) & \cos(\theta) \end{pmatrix}$ is the rotation operator with $\frac{\theta_1}{2}$ and θ_2 representing the rotation angles. If $R(\theta)$ acts on the input orthogonal states $|\uparrow\rangle = (1,0)^T$ and $|\downarrow\rangle = (0,1)^T$, the output state becomes a linear superposition of $|\uparrow\rangle$ and $|\downarrow\rangle$ with θ. $S = \begin{pmatrix} e^{i\epsilon} & 0 \\ 0 & e^{-i\epsilon} \end{pmatrix}$ is the phase shift operator, with a phase shift $e^{i\epsilon}$ ($e^{-i\epsilon}$) for state $|\uparrow\rangle$ ($|\downarrow\rangle$). In addition, because of the non-Hermiticity, each step contains gain-loss operators $G = \begin{pmatrix} e^{\gamma} & 0 \\ 0 & e^{-\gamma} \end{pmatrix}$ and $G^{-1} = \begin{pmatrix} e^{-\gamma} & 0 \\ 0 & e^{\gamma} \end{pmatrix}$, where γ is the gain-loss strength. Under the action of G, the wave function with the state $|\uparrow\rangle$ ($|\downarrow\rangle$) is amplified (reduced), while the effect of G^{-1} is opposite to that of G. The QW composed of the above operators satisfies parity-time (PT) symmetry. By selecting ϵ and θ_1 as parameters, the eigenvalues $\eta_{\pm} = e^{-i\lambda_{\pm}}$ of U_1 is obtained with the quasienergy $\lambda_{\pm}$. Calculation details are shown in Methods Section.

As depicted in Figure 1b ($\gamma = 0.2$ and $\theta_2 = \frac{\pi}{2}$), the degenerated quasienergies form two green ELs, separating PT-unbroken and PT-broken phases based on whether the quasienergies are real or imaginary. Furthermore, if we introduce the symmetry-breaking operator $\Psi = \begin{pmatrix} \cos(\varphi) & i\sin(\varphi) \\ i\sin(\varphi) & \cos(\varphi) \end{pmatrix}$ (the dotted box of Figure 1a) at each step, PT symmetry is broken when $\varphi \neq 0$. By solving the quasienergy $\lambda_{\pm}$ using θ_1 and φ, and setting $\varepsilon = 0$, an isolated EP (the green dot in Figure 1c) appears instead of ELs (see Methods Section). This enables us to conduct a comparative study of the physical phenomena around the EP and EL under the same theoretical framework.

The theory above can be experimentally observed through an all-optical QW platform. In Figure 1d, the two photons are generated at the β-BaB_2O_4 (BBO) crystals, one as a trigger and the other undergoing multiple-step QWs. The state $|\uparrow\rangle$ ($|\downarrow\rangle$) is encoded in the horizontal $|H\rangle$ (vertical $|V\rangle$) polarization. To implement the operator $R(\theta)$, a green half-wave plate (HWP) with 0^0 and a black HWP with θ are combined. Two quarter wave plates (QWPs) and one HWP are utilized to realize the operator S. Additionally, an equivalent gain-loss operator $L = \begin{pmatrix} l_1 & 0 \\ 0 & l_2 \end{pmatrix}$ with $\gamma = 1/2\ln(l_1/l_2)$ is used to represent the gain-loss operator G, where $0 \leq l_1, l_2 \leq 1$. The partial polarization beam splitter A (PPBS-A), with transmission coefficients of $(T_H, T_V) = (1, 0.45)$ for horizontal and vertical polarizations, is used to realize the operator L. Similarly, G^{-1} is implemented by the operator $L^{-1} = \begin{pmatrix} l_2 & 0 \\ 0 & l_1 \end{pmatrix}$ using a sandwich-type HWP-(PPBS-A)-HWP. Lastly, two QWPs and one HWP can achieve ψ. Realization details are provided in Experimental Section. For convenience, we denote each step of the PT-symmetric QW as $U_{PT,EL} = R(\frac{\theta_1}{2})GSR(\theta_2)G^{-1}SR(\frac{\theta_1}{2})$ corresponding to U_1 in Equation (1), and $U_{PT,EP} = \Psi U_{PT,EL}$ if Ψ is considered. Based on the platform above, the dynamic evolution of quantum states can be realized.

2.2. Dynamical Loop Evolution Around Exceptional Points or Exceptional Lines

In early studies, based on the adiabatic theorem, adiabatic evolution and the flip of two eigenstates can be obtained.[77–80] However, recent investigations have shown that gain and loss in non-Hermitian systems can lead to exponential amplification of small non-adiabatic couplings, i.e., the non-adiabatic transition (NAT), which obviously invalidates the adiabatic theorem. Thus, more general method need be adopted by directly solving the complete dynamical Schrödinger equations.[27–36] On the QW platform, our method corresponds to the latter. We consider two cases where the evolutionary direction is clockwise (**Figure 2a**) and counterclockwise (Figure 2d), respectively, with corresponding parameters identical to those in Figure 1c. The path equations for the nth step are $\varphi = R\cos(\pm\frac{2\pi}{N}n - \frac{\pi}{2})$ and $\theta_1 = R\sin(\pm\frac{2\pi}{N}n - \frac{\pi}{2}) + 1.1811$, where the radius $R = 0.38$ and the total step $N = 50$ ensure slow adiabatic evolution. The state evolves counterclockwise (clockwise) with a positive (negative) sign.

The state undergoing the nth step is denoted as $|X_n\rangle = C_G|X_G\rangle + C_L|X_L\rangle$, where $|X_G\rangle$ ($|X_L\rangle$) represent the instantaneous gain (loss) eigenstate with $Im(\lambda) > 0$ ($Im(\lambda) < 0$). When amplitude coefficients $|C_G| > |C_L|$ ($|C_G| < |C_L|$), the trajectory is marked on the gain (loss) surface, colored in red (blue). The state A (B) is chosen as the starting point, located at the upper (lower) energy sheet. When starting from state A clockwise, it initially evolves on the blue sheet, then jumps non-adiabatically to the red sheet (the white trajectory in Figure 2a). Finally, the state evolves into state A (Figure 2b). Whereas if starting from B, it remains on the red sheet and eventually evolves into state A (Figure 2c). For counterclockwise loops (Figure 2d), the final state is always state B regardless of the initial state, see Figure 2e, f. These results demonstrate the chiral state transfer on the QWs, which is consistent with previous studies.[27–33]

The corresponding experiments are performed with $N = 5$ (Figure 2g). The trends of the curves align with those results that satisfy the conditions of slow adiabatic evolution, indicating that such steps are sufficient. The red squares and blue circles in Figure 2g represent $|C_G|$ and $|C_L|$ in the experiment, consistent with the theoretical results. Due to losses in the experiment, the obtained matching counts decrease for higher step numbers. Thus, the error bars also become larger for higher step numbers.

Moreover, the conversion rate $P = \frac{|C_G|^2 - |C_L|^2}{|C_G|^2 + |C_L|^2}$ is provided to quantify the conversion of final evolved states.[38] $P = 1$ indicates the complete conversion of the state into the gain eigenstate, and vice versa. Larger R and fewer total steps are required to achieve a high conversion rate (Figure 2h). Related experimental details can be found in Experimental Section.

Now, we investigate the dynamical loop evolution in the system with ELs. Note that the loop parameters are not chosen on the EL, because at this point the eigenstates of the Hamiltonian become self-orthogonal and can no longer form the complete basis for the Hilbert space. The loop evolves in three ways: entirely in the PT-broken phase, encircling with EL, and entirely in the PT-unbroken phase. So when the loop encircles with EL, discrete parameter points (not on the EL) are chosen to form the loop. Here, we study the first case. The parameters are the same as those in Figure 1b, where $\theta_1 = R\cos(\pm\frac{2\pi}{N}n) + 1.56$ and $\varepsilon = R\sin(\pm\frac{2\pi}{N}n)$ with $R = 0.3$. It is important to emphasize that these values are not special, and the observed phenomena persist even if the parameters change. In the real part of energy spectrum, trajectories of different directions overlap completely. To distinguish the starting point and observe the evolution clearly, we provide the imaginary part in **Figure 3a** with the evolution trajectories in clockwise. The white trajectory represents the adiabatic evolution starting from state A. The entire evolution stays on the red sheet and eventually returns to the initial state (see Figure 3b), which is different from that in Figure 2a. When starting from state B, it initially evolves on the blue surface and then undergoes the NAT to the red surface, and eventually to state A, see Figure 3c. However, if the direction is counterclockwise (Figure 3d), the final state is always the gain state A, regardless of the initial state (Figure 3e,f).

Our theory is experimentally demonstrated in Figure 3g. Notably, the evolution around ELs exhibits a distinct behavior from the chiral behavior when encircling an EP. The final state is invariably the gain eigenstate, regardless of the input state or encircling direction. It attributes to different topologies of the Riemann surface between the EL system and the EP system. However, in the absence of EL or EP, there are not topological

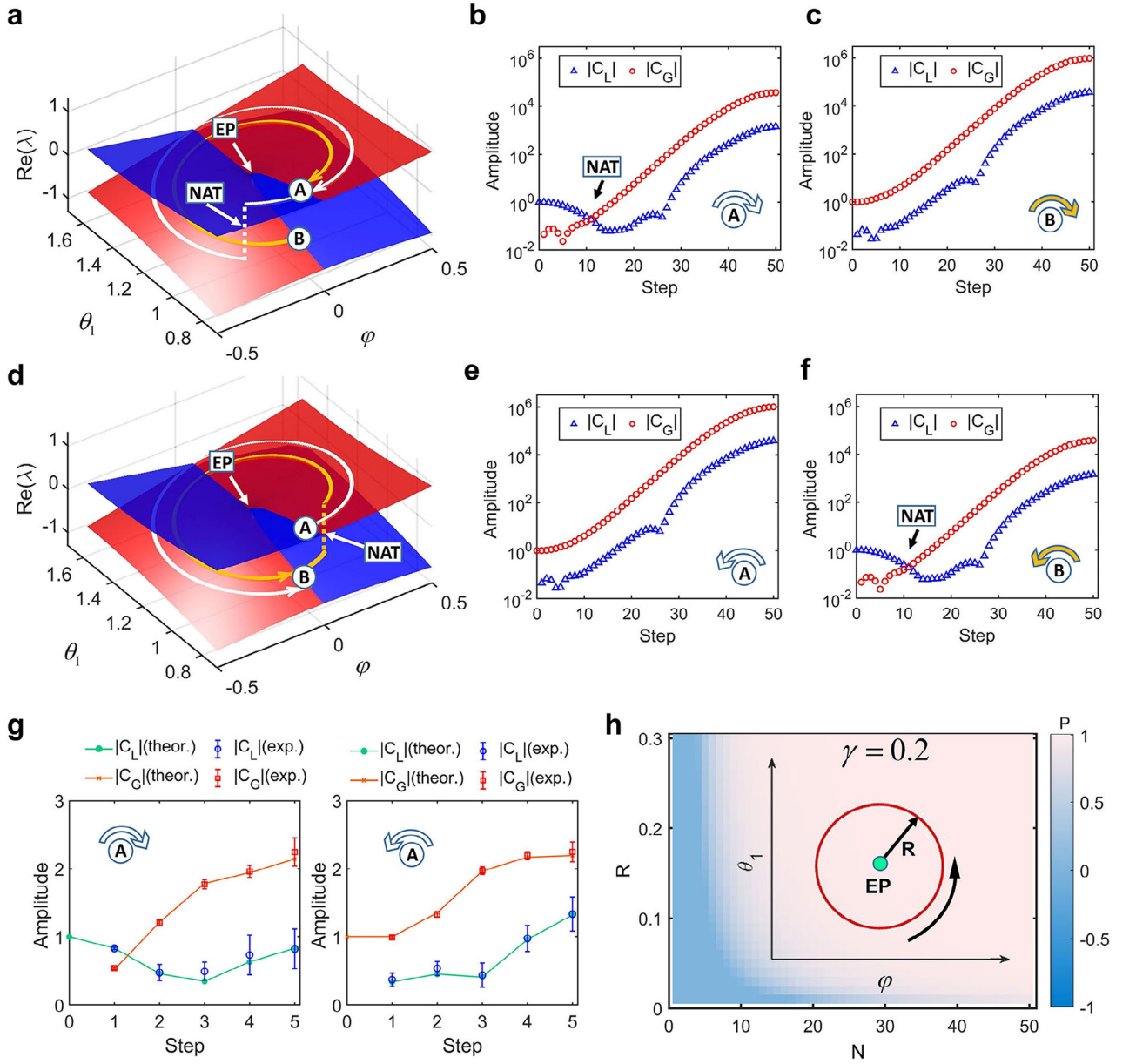

Figure 2. Dynamically encircling an EP driven by $U_{PT,EP}$. a,d) Trajectories on the Riemann surface in clockwise (counter-clockwise) around the EP. b,c,e,f) Amplitudes coefficients $|C_G|$ and $|C_L|$ in clockwise (counter-clockwise). g) Experimental results with $N = 5$. Error bars assume Poissonian photon-counting statistics. h) Conversion rate P of final states with the radius R and total step N. Insets show the evolution loop.

properties arising from the Riemann surface and non-Hermitian effect. In this case, after the eigenstate evolves around a closed loop, it returns to itself with only an accumulated phase, rather than transitioning to a different state.

Another difference between the EL and EP systems is the higher efficiency of quantum state transfer with ELs. As depicted in Figure 3h, with $R = 0.2$, the total step $N = 3$ is enough to guarantee the P approaching 1, whereas under the same conditions in Figure 2h, the total step N must be greater than 7 to reach the same P. Because the average overlap between the two eigenstates along the evolution loop in the EL system is higher, indicating that the distance between the two eigenstates is smaller. Therefore, dynamically encircling around ELs can significantly reduce the limitations of slow adiabatic conditions and achieve a more efficient state transfer. Besides the PT-broken phase, similar phenomena have been observed in the other two cases, see S1 of the Supporting Information.

Additionally, we investigate the dynamical loop evolution in the anti-parity-time (APT) symmetric QW. The realization of the APT-symmetric QW is put forward in Figure 1d. Detailed constructions of APT-symmetric QW possessing the EP ($U_{APT,EP}$) or EL ($U_{APT,EL}$), and derivations of eigenstates can be found in Methods Section. The analysis of dynamical loop evolution around EP or EL has been shown in S2 of Supporting

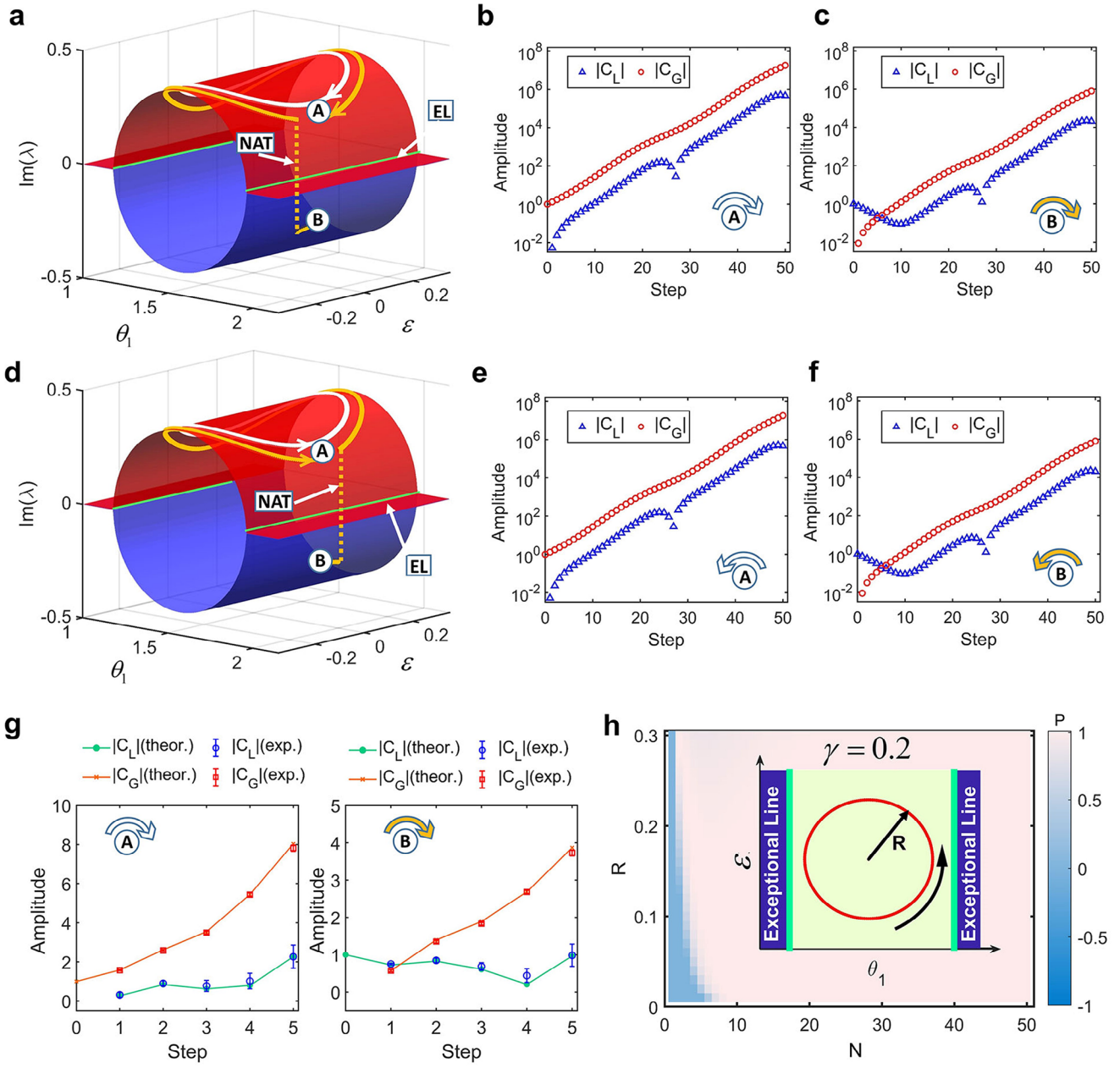

Figure 3. Dynamical loop evolution around ELs driven by $U_{PT,EL}$. a,d) Trajectories on the Riemann surface in clockwise (counter-clockwise) around the ELs. b,c,e,f) Amplitudes coefficients $|C_G|$ and $|C_L|$ in clockwise (counter-clockwise). g) Experimental results with $N = 5$. Error bars assume Poissonian photon-counting statistics. h) Conversion rate P of final states. Insets show the evolution loop.

Information. Similar as those discussions in the PT-symmetric QW above, it is found that the higher transfer efficiency has also been demonstrated in APT- symmetric QW with ELs. Notably, the state transfer around ELs has important applications, such as the robust generation of entangled states.

3. Experimental Realization of Robust Generation of Entanglement State

One common way to construct entangled states is through double-qubit gates, e.g., control-NOT (CNOT) gates.[81,82] However, the entangled states generated in this way are very reliant on incident quantum states and their fidelities are highly susceptible to environmental influences. By combining the quantum state transfer discussed above, we can effectively avoid the issues. Such a scheme is shown in **Figure** 4a, a pump light with polarization $|H\rangle$ is incident on the BBO crystal, generating two photons with polarization $|V\rangle$ through the type-I parametric down-conversion. Then these two photons are incident into the HWPs, followed by the transfer module with N-step QWs $U_{APT,EL} = GS(k)'R(\theta)'$, where $R' = e^{i\theta\sigma_y}$ and $S' = e^{i\epsilon\sigma_y}$ are the rotation operator and shift operator in the APT-symmetric

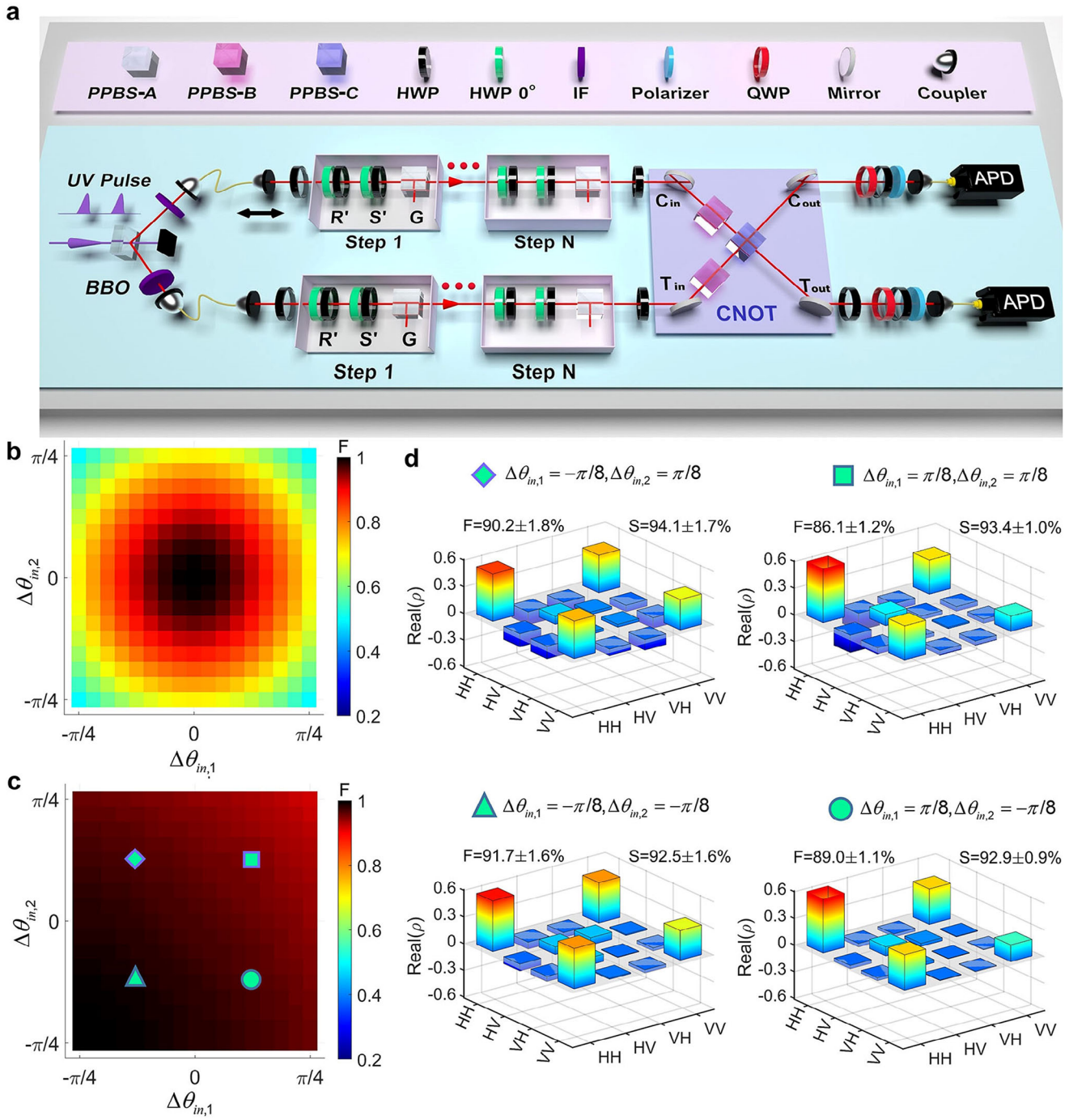

Figure 4. a) An experimental setup for entanglement state generation. The PPBS-A with transmission coefficients of $(T_H, T_V) = (1, 0.45)$ is used to realize the operator G. The CNOT gate is composed by three PPBSs, two PPBS-Bs have transmission coefficients of $(T_H, T_V) = (1, 0.67)$ for horizontal and vertical polarizations, and the PPBS-C has transmission coefficients of $(T_H, T_V) = (0, 0.67)$. b,c) The theoretical fidelity $F = \mathrm{tr}\sqrt{\rho_{\mathrm{bell}}{}^{1/2}\rho\rho_{\mathrm{bell}}{}^{1/2}}$ between the output state ρ and bell state $\rho_{\mathrm{bell}} = |\phi_{\mathrm{bell}}\rangle\langle\phi_{\mathrm{bell}}|$ without (with) passing through QWs. d) Experimental density matrices obtained by quantum state tomography.

system, respectively, and σ_y is the Pauli matrix. At the n-step, $\theta = 0.1\cos(\frac{2\pi}{N}n)$ and $\varepsilon = 0.1\sin(\frac{2\pi}{N}n)$. Before entering the transfer module, the two initial photons with $|V\rangle$ are prepared in state $|X_{\mathrm{L}}^0\rangle$ undergoing HWPs, where $|X_{\mathrm{L}}^0\rangle$ ($|X_{\mathrm{G}}^0\rangle$) is the instantaneous loss (gain) eigenstate of $U_{\mathrm{APT,EL}}$ with $n = 0$in θ and ε. Both states of photons convert to $|X_{\mathrm{G}}^0\rangle$ undergoing the transfer module, reflecting the NAT of non-Hermitian QWs. Then the upper and lower photons are prepared as $(|0\rangle_C + |1\rangle_C) \otimes |0\rangle_T$ with

HWPs after step N, where the upper (lower) photon denotes the control (target) qubit with $|0\rangle_C = |V\rangle_C$ and $|1\rangle_C = |H\rangle_C$ [$|0\rangle_T = \frac{1}{\sqrt{2}}(|V\rangle_T + |H\rangle_T)$ and $|1\rangle_T = \frac{1}{\sqrt{2}}(|V\rangle_T - |H\rangle_T)$]. Finally, these two photons are incident into the CNOT gate, and the entangled state $\frac{1}{\sqrt{2}}|V\rangle_C \otimes (|V\rangle_T + |H\rangle_T) + \frac{1}{\sqrt{2}}|H\rangle_C \otimes (|V\rangle_T - |H\rangle_T)$ is obtained undergoing the CNOT gate. By placing a HWP with $-\frac{\pi}{4}$ at the output port of target qubit, the state is converted into a bell state $|\phi_{\text{bell}}\rangle = \frac{1}{\sqrt{2}}(|V\rangle_C|V\rangle_T + |H\rangle_C|H\rangle_T)$. Experimental details about CNOT gate are provided in Experimental Section.

Compared with the conventional scheme, the above scheme has robustness to the change of the input state. To verify this feature, we change the rotation angles of the two HWPs before the step 1 through adding the perturbations $\Delta\theta_{\text{in},1}$ and $\Delta\theta_{\text{in},2}$ in the interval $(-\pi/4, \pi/4)$, which simulates external influences. In the conventional scheme, photons are directly incident to the CNOT gate without passing through N-step QWs. The fidelity decreases dramatically with the perturbation increasing, e.g., when $\Delta\theta_{\text{in},1} = \Delta\theta_{\text{in},2} = \pi/4$, the fidelity is already less than 0.5, see Figure 4b. In contrast, when both photons undergo 5-step QWs, the fidelity remains high for all perturbations. Even when $\Delta\theta_{\text{in},1} = \Delta\theta_{\text{in},2} = \pi/4$, the fidelity is still higher than 0.9, see Figure 4c. Therefore, our scheme is less sensitive to the input polarization than the conventional scheme. Furthermore, we add random perturbations to the path parameters θ and ϵ in the interval $(-0.05, 0.05)$, and obtain the average fidelity of entangled states still as high as 0.96 under 10 groups of perturbations, indicating a high tolerance to parameters. The reasons for these advantages are the non-Hermiticity and the special topology of the Riemann surface of the ELs system. Four representative points marked in Figure 4c are chosen to experimentally verify theoretical results. The experimental density matrices are presented in Figure 4d, and the average fidelities are close to 0.9. The similarity S ($S[\rho_{\text{th}}, \rho_{\text{ex}}] = \text{tr}\sqrt{\rho_{\text{th}}{}^{1/2}\rho_{\text{ex}}\rho_{\text{th}}{}^{1/2}}$, with theoretical (experimental) density matrices ρ_{th} (ρ_{ex})) is approximately 0.93 for each case.

4. Discussion and Conclusion

In conclusion, we have studied both theoretically and experimentally quantum state transfers around the ELs and EPs based on QW platforms. Comparing with the case around the EPs, we have found that evolutionary states around the ELs are independent of the initial states and evolution directions, and the transfers of quantum states are more efficient. In our selected parameters, the EL and EP systems have different Riemann surfaces, and the distance between the two eigenstates in the EL system is smaller than that in the EP system, so the loss eigenstates of the EL system need fewer steps to undergo the NAT accompanied by a strong gain effect. Based on these properties, we have constructed a method, and generated robust entangled states insensitive to the incident state experimentally. This robust generation of entangled states has great potentials in quantum information processing.

We would like to point out that similar behaviors for energy transfer should also appear although the above discussion is only about the quantum state transfer. In addition, the phenomena revealed by this work are also universal although the discussions above are based on the QW. In principle, the scheme can be implemented on any platform, such as waveguides, integrated chips and so on. Thus, our work may inspire further researches on the dynamical encircling process around the ELs in many other branches of physics, such as acoustics, optics and electron systems.

5. Methods

5.1. The Derivation of Symmetry

5.1.1. Parity-Time Reversal Symmetry

For $U_{\text{PT,EL}} = R(\frac{\theta_1}{2})\text{GSR}(\theta_2)G^{-1}\text{SR}(\frac{\theta_1}{2})$, the coin, conditional shift, and gain-loss operators can be rewritten as $R(\theta) = e^{-i\theta\sigma_y}$, $S = e^{i\epsilon\sigma_z}$, $G = e^{\gamma\sigma_z}$, $G^{-1} = e^{-\gamma\sigma_z}$. Then the evolution operator can be expressed as $U_{\text{PT,EL}} = e^{-i\frac{\theta_1}{2}\sigma_y}e^{\gamma\sigma_z}e^{i\epsilon\sigma_z}e^{-i\theta_2\sigma_y}e^{-\gamma\sigma_z}e^{i\epsilon\sigma_z}e^{-i\frac{\theta_1}{2}\sigma_y}$. We introduce the PT-symmetric operator $\text{PT} = \sigma_z K$, where the operators K and σ_z represent the complex conjugate operator and the Pauli matrix along the z direction, respectively. Consequently, we can calculate and obtain the following relation:

$$(PT)\, U_{\text{PT,EL}}(\text{PT})^{-1} = e^{i\frac{\theta_1}{2}\sigma_y}e^{\gamma\sigma_z}e^{-i\epsilon\sigma_z}e^{i\theta_2\sigma_y}e^{-\gamma\sigma_z}e^{-i\epsilon\sigma_z}e^{i\frac{\theta_1}{2}\sigma_y},$$
$$(PT)\, U_{\text{PT,EL}}(PT)^{-1}U_{\text{PT,EL}} = I \tag{2}$$

where I is the identity matrix. The above non-Hermitian evolution operator satisfies $(\text{PT})\, U_{\text{PT,EL}}(PT)^{-1} = {U_{PT,EL}}^{-1}$, thus $U_{PT,EL}$ possesses parity-time reversal symmetry. For the evolution operator $U_{\text{PT,EP}} = \Psi(\varphi)U_{\text{PT,EL}}$, the system is PT-symmetric only when $\varphi = 0$.

5.1.2. Anti-Parity-Time Reversal Symmetry

We first consider the symmetry of the operator $U = e^{i\theta\sigma_x}e^{i\epsilon\sigma_x}e^{\gamma\sigma_z}$. By introducing the PT-symmetric operator $PT = \sigma_z K$, the equation can be calculated as follows:

$$(\text{PT})\, e^{i\theta\sigma_x}(PT)^{-1} = e^{i\theta\sigma_x}, (\text{PT})\, e^{i\epsilon\sigma_x}(PT)^{-1}$$
$$= e^{i\epsilon\sigma_x}, (\text{PT})\, e^{\gamma\sigma_z}(\text{PT})^{-1} = e^{\gamma\sigma_z} \tag{3}$$

So $(\text{PT})\, U(\text{PT})^{-1} = U$, and U satisfies anti-parity-time reversal symmetry. For the convenience of experimental implementation, we make a translation operation. The expression of the PT symmetry operator is chosen as $\text{PT}' = \sigma_0 K$, and the evolution operator after the translation is $U_{\text{APT,EL}} = e^{\gamma\sigma_z}e^{i\epsilon\sigma_y}e^{i\theta\sigma_y} = \text{GS}'R'$, where $R' = e^{i\theta\sigma_y}$, $S' = e^{i\epsilon\sigma_y}$, and $G = e^{\gamma\sigma_z}$ correspond to the coin, conditional shift, and gain-loss operators respectively. The following relation can be obtained:

$$\left(\text{PT}'\right) R'\left(\text{PT}'\right)^{-1} = e^{i\theta\sigma_y}, \left(\text{PT}'\right) S'\left(\text{PT}'\right)^{-1}$$
$$= e^{i\epsilon\sigma_y}, \left(PT'\right) G\left(PT'\right)^{-1} = e^{\gamma\sigma_z} \tag{4}$$

It is obvious to get the relation $(\text{PT}')\, U_{\text{APT,EL}}(\text{PT}')^{-1} = U_{\text{APT,EL}}$, thus the evolution operator $U_{\text{APT,EL}}$ obeys anti-parity-time reversal symmetry. For the evolution operator $U_{\text{APT,EP}} = \Psi'(\varphi)U_{\text{APT,EL}}$ with $\Psi'(\varphi) = e^{i\varphi\sigma_z}$, the system is APT-symmetric only when $\varphi = 0$.

5.2. The Eigenvalues and Eigenvectors of QWs Possessing EP and EL

In this section, we provide the solutions for the energy eigenvalues and eigenvectors. In the process, the time-evolution operator $U_{\mathrm{PT,EL}} = R(\frac{\theta_1}{2})\mathrm{GSR}(\theta_2)G^{-1}\mathrm{SR}(\frac{\theta_1}{2})$ can be expressed by an identity matrix σ_0, Pauli matrices σ_x, σ_y and σ_z as

$$\begin{aligned} U_{\mathrm{PT,EL}} &= d_0\sigma_0 + d_x\sigma_x + id_y\sigma_y + id_0\sigma_z = \begin{pmatrix} d_0 + id_z & d_x + d_y \\ d_x - d_y & d_0 - id_z \end{pmatrix} d_0 \\ &= \cos 2\varepsilon \cos\theta_1 \cos\theta_2 - \cos h2\gamma \sin\theta_1 \sin\theta_2, d_x \\ &= -\sin h2\gamma \sin\theta_2, d_y = -\cos\theta_2 \sin\theta_1 \cos 2\varepsilon \\ &\quad - \cos h2\gamma \cos\theta_1 \sin\theta_2, d_z = \cos\theta_2 \sin 2\varepsilon \end{aligned} \tag{5}$$

where the relation ${d_0}^2 - {d_x}^2 + {d_y}^2 + {d_z}^2 = 1$ is satisfied. Then, we can calculate the eigenvalues $\eta_\pm = d_0 \pm \sqrt{{d_0}^2 - 1} = e^{-i\lambda}$, where λ is the quasienergy. When ${d_0}^2 = 1$, the eigenvalues are degenerate. Therefore, we can solve the positions of the ELs. The left and right eigenvectors of $U_{\mathrm{PT,EL}}$ satisfy the relation $U_{\mathrm{PT,EL}}|\alpha\rangle = \eta|\alpha\rangle$, ${U_{\mathrm{PT,EL}}}^\dagger|\beta\rangle = \eta^*|\beta\rangle$, which are solved to be

$$\begin{aligned} |\alpha_\pm\rangle &= \frac{1}{\sqrt{(2\eta_\pm - 2d_0)(d_x + d_y)}} \begin{pmatrix} d_x + d_y \\ \eta_\pm - d_0 - id_z \end{pmatrix} \langle\beta_\pm| \\ &= \frac{1}{\sqrt{(2\eta_\pm - 2d_0)(d_x + d_y)}} \begin{pmatrix} \eta_\pm - d_0 + id_z \\ d_x + d_y \end{pmatrix}^T \end{aligned} \tag{6}$$

For the time-evolution operator $U_{\mathrm{PT,EP}} = \Psi U_{\mathrm{PT,EL}}$, we assume $U_{\mathrm{PT,EL}} = \begin{pmatrix} a & b \\ c & d \end{pmatrix}$, $U_{\mathrm{PT,EP}} = \Psi U_{\mathrm{PT,EL}} = \begin{pmatrix} a\cos(\varphi) + ic\sin(\varphi) & b\cos(\varphi) + id\sin(\varphi) \\ c\cos(\varphi) + ia\sin(\varphi) & d\cos(\varphi) + ib\sin(\varphi) \end{pmatrix}$. Then the eigenvalues cans be calculated as $\eta_\pm = M \pm \sqrt{M^2 - 1} = e^{-i\lambda}$, where $M = \frac{(a+d)\cos(\varphi) + (b+c)i\sin(\varphi)}{2}$. When $M^2 = 1$, the eigenvalues are degenerate. Therefore, we can solve the positions of the EPs. The left and right eigenvectors of $U_{\mathrm{PT,EP}}$ satisfy the relation $U_{\mathrm{PT,EP}}|\alpha\rangle = \eta|\alpha\rangle$ and ${U_{\mathrm{PT,EP}}}^\dagger|\beta\rangle = \eta^*|\beta\rangle$, which are solved to be

$$\begin{aligned} |\alpha_\pm\rangle &= \frac{1}{\sqrt{(2\eta_\pm - 2M)(b\cos(\varphi) + id\sin(\varphi))}} \\ &\quad \begin{pmatrix} b\cos(\varphi) + id\sin(\varphi) \\ \eta_\pm - a\cos(\varphi) - ic\sin(\varphi) \end{pmatrix} \langle\beta_\pm| \\ &= \frac{1}{\sqrt{(2\eta_\pm - 2M)(b\cos(\varphi) + id\sin(\varphi))}} \\ &\quad \begin{pmatrix} \eta_\pm - d\cos(\varphi) - ib\sin(\varphi) \\ b\cos(\varphi) + id\sin(\varphi) \end{pmatrix}^T \end{aligned} \tag{7}$$

In the discussion, we also consider the loop evolution in the QW possessing anti-parity-time (APT) symmetry. First, when the ELs appear in the spectrum of APT-symmetric QW, the time-evolution operator is $U_{\mathrm{APT,EL}} = \mathrm{GS}'R' = \begin{pmatrix} e^\gamma\cos(\varepsilon+\theta) & e^\gamma\sin(\varepsilon+\theta) \\ -e^{-\gamma}\sin(\varepsilon+\theta) & e^{-\gamma}\cos(\varepsilon+\theta) \end{pmatrix}$. We can calculate the eigenvalues $\eta_\pm = M \pm \sqrt{M^2 - 1} = e^{-i\lambda}$, where $M = \cos h(\gamma)\cos(\varepsilon+\theta)$. Similarly, we assume the relationship $U_{\mathrm{APT,EL}} = \begin{pmatrix} a' & b' \\ c' & d' \end{pmatrix}$, The left and right eigenvectors of $U_{\mathrm{APT,EL}}$ satisfy the relation $U_{\mathrm{APT,EL}}|\alpha\rangle = \eta|\alpha\rangle$ and ${U_{\mathrm{APT,EL}}}^\dagger|\beta\rangle = \eta^*|\beta\rangle$, which are solved to be

$$\begin{aligned} |\alpha_\pm\rangle &= \frac{1}{\sqrt{(2\eta_\pm - 2M)\,b}} \begin{pmatrix} b' \\ \eta_\pm - a' \end{pmatrix}, \langle\beta_\pm| \\ &= \frac{1}{\sqrt{(2\eta_\pm - 2M)\,b}} \begin{pmatrix} \eta_\pm - d' \\ b' \end{pmatrix}^T \end{aligned} \tag{8}$$

When the APT-symmetric QW has EPs in its spectrum, the evolution operator is $U_{\mathrm{APT,EP}} = \Psi' U_{\mathrm{APT,EL}} = \begin{pmatrix} e^{i\varphi} & 0 \\ 0 & e^{-i\varphi} \end{pmatrix} \begin{pmatrix} e^\gamma\cos(\varepsilon+\theta) & e^\gamma\sin(\varepsilon+\theta) \\ -e^{-\gamma}\sin(\varepsilon+\theta) & e^{-\gamma}\cos(\varepsilon+\theta) \end{pmatrix}$. The eigenvalues can be calculated as $\eta_\pm = M \pm \sqrt{M^2 - 1} = e^{-i\lambda}$, where $M = \cos h(\gamma + i\varphi)\cos(\varepsilon+\theta)$. Similarly, we assume the relationship $U_{\mathrm{APT,EP}} = \begin{pmatrix} a'' & b'' \\ c'' & d'' \end{pmatrix}$. The left and right eigenvectors of $U_{\mathrm{APT,EP}}$ are solved to be

$$\begin{aligned} |\alpha_\pm\rangle &= \frac{1}{\sqrt{(2\eta_\pm - 2M)\,be^{i\varphi}}} \begin{pmatrix} b''e^{i\varphi} \\ \eta_\pm - a''e^{i\varphi} \end{pmatrix} \langle\beta_\pm| \\ &= \frac{1}{\sqrt{(2\eta_\pm - 2M)\,be^{i\varphi}}} \begin{pmatrix} \eta_\pm - d''e^{-i\varphi} \\ b''e^{i\varphi} \end{pmatrix}^T \end{aligned} \tag{9}$$

6. Experimental Section

Experimental Realization of Operators: The Jones matrices of the HWP and QWP are $\mathrm{HWP}(\zeta) = \begin{pmatrix} \cos(\zeta) & \sin(\zeta) \\ \sin(\zeta) & -\cos(\zeta) \end{pmatrix}$ and $\mathrm{QWP}(\zeta) = \frac{\sqrt{2}}{2}\begin{pmatrix} 1 - i\cos(\zeta) & -i\sin(\zeta) \\ -i\sin(\zeta) & 1 + i\cos(\zeta) \end{pmatrix}$ are used. It is worth noting that the actual rotation angle in the experiment is $\frac{\zeta}{2}$. Theoretically, the combination of two QWPs and one HWP can realize any unitary operation of single polarization bits. In the specific experimental design, the above-mentioned universal combination of waveplates is not used for the unitary evolution with a special structure (e.g., the unitary evolution matrix can be realized by two HWPs), but design a specific combination of waveplates to achieve a more concise and intuitive form of this evolution. In the design of wave plate group, sometimes the unitary evolution formed by a combination of waveplates is not completely equivalent to the target unitary evolution but adds a global phase to the evolution result. In fact, adding a global phase to a state does not change the meaning of the state. Therefore, under the theory of quantum mechanics, it can be considered that the unitary evolution realized by this group of wave plates is completely equivalent to the unitary evolution of the target.

a. Realization of R.

$$R(\theta) = \begin{pmatrix} \cos(\theta) & -\sin(\theta) \\ \sin(\theta) & \cos(\theta) \end{pmatrix} = \begin{pmatrix} \cos(\theta) & \sin(\theta) \\ \sin(\theta) & -\cos(\theta) \end{pmatrix} \begin{pmatrix} 1 & 0 \\ 0 & -1 \end{pmatrix} = \mathrm{HWP}(\theta)\,\mathrm{HWP}(0) \tag{10}$$

The rotation operator R can be achieved by the combination of two half-wave pieces with angles 0 and θ respectively.

b. Realization of S.

$$S = \begin{pmatrix} e^{i\varepsilon} & 0 \\ 0 & e^{-i\varepsilon} \end{pmatrix} = i\frac{\sqrt{2}}{2}\begin{pmatrix} 1 & -i \\ -i & 1 \end{pmatrix}\begin{pmatrix} \sin(\varepsilon) & \cos(\varepsilon) \\ \cos(\varepsilon) & -\sin(\varepsilon) \end{pmatrix}\frac{\sqrt{2}}{2}\begin{pmatrix} 1 & -i \\ -i & 1 \end{pmatrix} = e^{i\frac{\pi}{2}}\mathrm{QWP}\left(\frac{\pi}{2}\right)\mathrm{HWP}\left(\frac{\pi}{2}-\varepsilon\right)\mathrm{QWP}\left(\frac{\pi}{2}\right) \tag{11}$$

Therefore, the operator S can be realized by combining two QWPs with an angle of $\frac{\pi}{2}$ and one HWP with an angle of $\frac{\pi}{2}-\varepsilon$.

c. Realization of L and L'. For the polarization-dependent loss operators $L = \begin{pmatrix} l_1 & 0 \\ 0 & l_2 \end{pmatrix}$ and $L' = \begin{pmatrix} l_2 & 0 \\ 0 & l_1 \end{pmatrix}$, they are implemented using a partial polarization beam splitter (PPBS), an optical device with different transmittance $(t_H, t_V) = (l_1^2, l_2^2)$ for the horizontal and vertical polarization of the incident light. In the experiment, the horizontal polarization can be fully transmitted ($t_H = l_1^2 = 1$), while the vertical polarization has a transmittance ($t_V = l_2^2$), which implements the polarization-controlled loss operators. The gain-loss intensity $\gamma = 1/2\ln(l_1/l_2)$ chosen in the experimental procedure is equal to 0.2, so the corresponding transmittance parameter of our customized PPBS-A is $(l_1^2, l_2^2) = (1, 0.45)$. Similarly, the loss operator L' can be achieved by a PPBS-A with another type of transmittance $(t_H, t_V) = (l_2^2, l_1^2)$. In order to realize such a PPBS-A with a special polarization transmittance, two HWPs are inserted with a rotation angle of $\frac{\pi}{4}$ before and after the light is incident on the PPBS-A. In this way, the loss operator L' can be experimentally realized by an optical device with a sandwich-type HWP-(PPBS-A)-HWP combination.

d. Realization of Ψ.

$$\Psi = \begin{pmatrix} \cos(\varphi) & i\sin(\varphi) \\ i\sin(\varphi) & \cos(\varphi) \end{pmatrix} = i\frac{1}{2}\begin{pmatrix} 1-i & 0 \\ 0 & 1+i \end{pmatrix}\begin{pmatrix} \cos(\varphi) & \sin(\varphi) \\ \sin(\varphi) & -\cos(\varphi) \end{pmatrix}\begin{pmatrix} 1-i & 0 \\ 0 & 1+i \end{pmatrix} = e^{i\frac{\pi}{2}}\mathrm{QWP}(0)\,\mathrm{HWP}(\varphi)\,\mathrm{QWP}(0) \tag{12}$$

It is obvious that the operator Ψ can be realized by combining two QWPs with an angle of 0 and one HWP with an angle of φ.

e. Realization of S' and R'.

$$R' = \begin{pmatrix} \cos(\theta) & \sin(\theta) \\ -\sin(\theta) & \cos(\theta) \end{pmatrix} = \begin{pmatrix} \cos(\theta) & -\sin(\theta) \\ -\sin(\theta) & -\cos(\theta) \end{pmatrix}\begin{pmatrix} 1 & 0 \\ 0 & -1 \end{pmatrix} = \mathrm{HWP}(-\theta)\,\mathrm{HWP}(0) \tag{13}$$

The expression of operator S' is the same as that of R', so they can be achieved by the combination of two half-wave pieces with angles 0 and $-(\theta+\varepsilon)$ respectively.

f. Realization of Ψ'.

$$\Psi' = \begin{pmatrix} e^{i\varphi} & 0 \\ 0 & e^{-i\varphi} \end{pmatrix} = i\frac{\sqrt{2}}{2}\begin{pmatrix} 1 & -i \\ -i & 1 \end{pmatrix}\begin{pmatrix} \sin(\varphi) & \cos(\varphi) \\ \cos(\varphi) & -\sin(\varphi) \end{pmatrix}\frac{\sqrt{2}}{2}\begin{pmatrix} 1 & -i \\ -i & 1 \end{pmatrix} = e^{i\frac{\pi}{2}}\mathrm{QWP}\left(\frac{\pi}{2}\right)\mathrm{HWP}\left(\frac{\pi}{2}-\varphi\right)\mathrm{QWP}\left(\frac{\pi}{2}\right) \tag{14}$$

Therefore, the operator Ψ' can be realized by combining two QWPs with an angle of $\frac{\pi}{2}$ and one HWP with an angle of $\frac{\pi}{2}-\varphi$.

Highly Efficient Transfer of Quantum State: Besides the polarization-dependent loss caused by the PPBS, there is also a general loss due to imperfect optical components. In the experiment, the input parameters including θ_1 are implemented by rotating the half-wave or quarter-wave plates to specific angles. The accuracy is determined by the graduation value of the scale, reaching 1°. the transmittance of each HWP and QWP used was approximately 0.986. The measured general loss rate in each step of the walk was approximately 0.144, and after undergoing five steps of the quantum walk, the probability of successfully obtaining photons was only 0.06. It is measured that the coincidence counts of matching pairs of photons directly generated from BBO can reach approximately 3×10^3 per second. For the evolution operator $U_{PT,EP}$, when the initial state A evolves in a counterclockwise direction (Figure 2a), it is measured that the count of matching pairs decays to only about 1.8×10^2 per second after 5 steps, indicating that most of the photons are lost. During the measurement process, the number of times was recorded the signal photon detector and the idle photon detector responded with a match. When a coincidence count is received, it represents the successful completion of the photon's cyclic evolution. In the complete state tomography of a single-photon state, four measurement bases were set up and recorded the total number of coincidences between the signal and idle photons in 10 s for each basis and repeated it 10 times to obtain one data point.

Robust Generation of Entanglement State: 400 nm picosecond laser pulses were first used to pump a 3 mm thick BBO crystal, generating time-correlated 800 nm photon pairs through the type-I parametric down-conversion process. These photon pairs were passed through interference filters to enhance their indistinguishability and coupled into single-mode fibers before being delivered to the N-step APT-symmetric QWs with ELs. The QWs system is described by the evolution operators $U_{APT} = \mathrm{GS}(\varepsilon)'R(\theta)'$ satisfying the APT symmetry. The evolution loop equations chosen are $\theta = 0.1\cos(\frac{2\pi}{N}n)$ and $\varepsilon = 0.1\sin(\frac{2\pi}{N}n)$, state $|X_G^0\rangle$ and $|X_L^0\rangle$ are defined as the eigenstates of gain and loss when $n = 0$. The initial photons with polarization $|V\rangle$ in the upper and lower paths are prepared in state $|X_L^0\rangle$ after the action of the HWP before step 1, and are both converted to state $|X_G^0\rangle$ after experiencing the same QWs evolution loop. Finally, both two photons in state $|X_G^0\rangle$ are prepared as $\frac{1}{\sqrt{2}}(|V\rangle_T + |H\rangle_T)$ by the HWP after step N and then incident into the CNOT gate, with the upper photon as the control qubit and the lower photon as the target qubit.

The computational basis of the CNOT gate are defined as $|0\rangle_C = |V\rangle_C, |1\rangle_C = |H\rangle_C$ for the control qubit and $|0\rangle_T = \frac{1}{\sqrt{2}}(|V\rangle_T + |H\rangle_T), |1\rangle_T = \frac{1}{\sqrt{2}}(|V\rangle_T - |H\rangle_T)$ for the target qubit. Therefore, the incident state before the CNOT gate can be expressed as a direct product state $(|0\rangle_C + |1\rangle_C) \otimes |0\rangle_T$. The entangled state $\frac{1}{\sqrt{2}}|V\rangle_C \otimes (|V\rangle_T + |H\rangle_T) + \frac{1}{\sqrt{2}}|H\rangle_C \otimes (|V\rangle_T - |H\rangle_T)$ can be obtained after the action of the CNOT gate. To make the density matrix more intuitive, the two-photon state can be converted into the form of a bell state $\frac{1}{\sqrt{2}}(|V\rangle_C|V\rangle_T + |H\rangle_C|H\rangle_T)$ by placing a half wave plate with a rotation angle of $-\frac{\pi}{4}$ at the output port of target qubit. In this way, the bell state can be generated. Such a CNOT gate is experimentally implemented by a combination of three PPBSs. The central PPBS-C implements an entangling gate operation by reflecting vertically polarized light perfectly and reflecting (transmitting) 1/3 (2/3) of horizontally polarized light. The two PPBS-Bs are inserted to adjust the amplitudes of the photonic qubits by transmitting (reflecting) 1/3 (2/3) of vertically polarized light and transmitting horizontally polarized light perfectly. Due to the effect of the beam splitter with a reflection rate of 1/3, both photons are lost, so the success of this CNOT gate is not deterministic. The success probability of this all-optical CNOT gate is 1/9. However, once the final state (coincidence counts of the control and target qubits) is successfully detected, it represents the successful implementation of the controlled-NOT gate. Finally, after passing through the projection measurement device composed of HWP, QWP, and polarizers, the two photons are coupled into a fiber and imported into a single-photon detector. During the measurement, the number of matching detector responses of the two photons is only recorded. By measuring the coincidence counts for 16

different sets of measurement bases, the complete state tomography was achieved and the density matrix was reconstructed.

Adjustment of the Two-Photon Interferometer: The experimental implementation of the CNOT gate is based on Hong-Ou-Mandel (HOM) interference, which is a two-photon interference effect in quantum optics, and its phenomenon originates from the full homogeneity of bosons. In order to adjust the two-photon interferometer, the incident light of both paths to be horizontally polarized is regulated, and when the incident state is $|H_aH_b\rangle$, there are only two cases when the two-photon coincidence counting can be got: the two photons are transmitted and reflected at the same time. However, the simultaneous reflection will produce a relative phase of π, accordingly, this process can be written as the following expression:

$$|H_aH_b\rangle \overset{\text{PPBS-C}}{\rightarrow} \sqrt{\frac{2}{3}} \times \sqrt{\frac{2}{3}} |H_dH_c\rangle - \frac{1}{\sqrt{3}} \times \frac{1}{\sqrt{3}} |H_cH_d\rangle \tag{15}$$

For large delays, the two photons are completely distinguishable due to their time of arrival. The output state is $\frac{2}{3}|H_dH_c\rangle - \frac{1}{3}|H_cH_d\rangle$. The probability to get a coincidence is $\frac{5}{9}$. For zero delay, the two photons are perfectly indistinguishable, the output state is $\frac{1}{3}|HH\rangle$ because of probability amplitude cancellation and the probability is reduced to $\frac{1}{9}$. In the experiment, in order to adjust the optical path difference of the two photons, the coupling head installed on the translation platform is moved. After measurement, the HOM curve is obtained. Two-photon coincidence counts are shown as red circles and the blue line shows a fit to this data with Gaussian. The existence of HOM dip can be clearly observed and the two-photon interferometer can be well adjusted when the coincidence counts are minimum.

Supporting Information

Supporting Information is available from the Wiley Online Library or from the author.

Acknowledgements

Z.T. and T.C. contributed equally to this work. This work was supported by the National Key R & D Program of China under Grant No. 2022YFA1404904 and the National Natural Science Foundation of China (12234004, 11974046 and 12374323).

Conflict of Interest

The authors declare no conflict of interest.

Data Availability Statement

The data that support the findings of this study are available from the corresponding author upon reasonable request.

Keywords

chiral state transfer, exceptional point and exceptional line, nonadiabatic transition, quantum walk, robust generation of entanglement state

Received: August 20, 2023
Revised: November 5, 2023
Published online: November 23, 2023

[1] R. El-Ganainy, K. G. Makris, M. Khajavikhan, Z. H. Musslimani, S. Rotter, D. N. Christodoulides, *Nat. Phys.* **2018**, *14*, 11.
[2] L. Feng, R. El-Ganainy, L. Ge, *Nat. Photonics* **2017**, *11*, 752.
[3] S. K. Özdemir, S. Rotter, F. Nori, L. Yang, *Nat. Mater.* **2019**, *18*, 783.
[4] M.-A. Miri, A. Alù, *Science* **2019**, *363*, eaar7709.
[5] E. J. Bergholtz, J. C. Budich, F. K. Kunst, *Rev. Mod. Phys.* **2021**, *93*, 015005.
[6] M. Parto, Y. G. N. Liu, B. Bahari, M. Khajavikhan, D. N. Christodoulides, *Nanophotonics* **2021**, *10*, 403.
[7] Q.i Zhong, M. Khajavikhan, D. N. Christodoulides, R. El-Ganainy, *Nat. Commun.* **2018**, *9*, 4808.
[8] C. M. Bender, S. Boettcher, *Phys. Rev. Lett.* **1998**, *80*, 5243.
[9] Y. Choi, S. Kang, S. Lim, W. Kim, J.-R. Kim, J.-H. Lee, K. An, *Phys. Rev. Lett.* **2010**, *104*, 153601.
[10] T. Gao, E. Estrecho, K. Y. Bliokh, T. C. H. Liew, M. D. Fraser, S. Brodbeck, M. Kamp, C. Schneider, S. Höfling, Y. Yamamoto, F. Nori, Y. S. Kivshar, A. G. Truscott, R. G. Dall, E. A. Ostrovskaya, *Nature* **2015**, *526*, 554.
[11] C. E. Rüter, K. G. Makris, R. El-Ganainy, D. N. Christodoulides, M. Segev, D. Kip, *Nat. Phys.* **2010**, *6*, 192.
[12] A. Regensburger, C. Bersch, M.-A. Miri, G. Onishchukov, D. N. Christodoulides, U. Peschel, *Nature* **2012**, *488*, 167.
[13] B.o Peng, S. K. Özdemir, F. Lei, F. Monifi, M. Gianfreda, G. L.u Long, S. Fan, F. Nori, C. M. Bender, L. Yang, *Nat. Phys.* **2014**, *10*, 394.
[14] K. Ding, G. Ma, M. Xiao, Z. Q. Zhang, C. T. Chan, *Phys. Rev. X* **2016**, *6*, 021007.
[15] S. Weimann, M. Kremer, Y. Plotnik, Y. Lumer, S. Nolte, K. G. Makris, M. Segev, M. C. Rechtsman, A. Szameit, *Nat. Mater.* **2017**, *16*, 433.
[16] L. Xiao, X. Zhan, Z. H. Bian, K. K. Wang, X. Zhang, X. P. Wang, J. Li, K. Mochizuki, D. Kim, N. Kawakami, W. Yi, H. Obuse, B. C. Sanders, P. Xue, *Nat. Phys.* **2017**, *13*, 1117.
[17] T. E. Lee, *Phys. Rev. Lett.* **2016**, *116*, 133903.
[18] H. Shen, B. Zhen, L. Fu, *Phys. Rev. Lett.* **2018**, *120*, 146402.
[19] K. Kawabata, K. Shiozaki, M. Ueda, M. Sato, *Phys. Rev.* **2019**, *X9*, 041015.
[20] L. Xiao, T. Deng, K. Wang, G. Zhu, Z. Wang, W. Yi, P. Xue, *Nat. Phys.* **2020**, *16*, 761.
[21] T. Helbig, T. Hofmann, S. Imhof, M. Abdelghany, T. Kiessling, L. W. Molenkamp, C. H. Lee, A. Szameit, M. Greiter, R. Thomale, *Nat. Phys.* **2020**, *16*, 747.
[22] B.o Wang, T. Chen, X. Zhang, *Laser Photonics Rev.* **2020**, *14*, 2000092.
[23] L.i Ge, H. E. Türeci, *Phys. Rev. A* **2013**, *88*, 053810.
[24] Y. Li, Y.u-G. Peng, L. Han, M.-A. Miri, W. Li, M. Xiao, X.-F. Zhu, J. Zhao, A. Alù, S. Fan, C.-W. Qiu, *Science* **2019**, *364*, 170.
[25] F. Minganti, V. Macrì, A. Settineri, S. Savasta, F. Nori, *Phys Rev A* **2021**, *103*, 052201.
[26] R. Huang, S. K. Özdemir, J.-Q. Liao, F. Minganti, L.e-M. Kuang, F. Nori, H. Jing, *Laser Photonics Rev.* **2022**, *16*, 2100430.
[27] R. Uzdin, A. Mailybaev, N. Moiseyev, *J. Phys. A* **2011**, *44*, 435302.
[28] I. Gilary, A. A. Mailybaev, N. Moiseyev, *Phys. Rev. A* **2013**, *88*, 010102.
[29] T. J. Milburn, J. Doppler, C. A. Holmes, S. Portolan, S. Rotter, P. Rabl, *Phys. Rev. A* **2015**, *92*, 052124.
[30] H. Xu, D. Mason, L. Jiang, J. G. E. Harris, *Nature* **2016**, *537*, 80.
[31] J. Doppler, A. A. Mailybaev, J. Böhm, U. Kuhl, A. Girschik, F. Libisch, T. J. Milburn, P. Rabl, N. Moiseyev, S. Rotter, *Nature* **2016**, *537*, 76.
[32] A. U. Hassan, B.o Zhen, M. Soljacic, M. Khajavikhan, D. N. Christodoulides, *Phys. Rev. Lett.* **2017**, *118*, 093002.
[33] J. W. Yoon, Y. Choi, C. Hahn, G. Kim, S. H.o Song, K.i-Y. Yang, J. Y. Lee, Y. Kim, C. S. Lee, J. K. Shin, H.-S. Lee, P. Berini, *Nature* **2018**, *562*, 86.
[34] M. Naghiloo, M. Abbasi, Y. N. Joglekar, K. W. Murch, *Nat. Phys.* **2019**, *15*, 1232.
[35] X.-L. Zhang, T. Jiang, C. T. Chan, *Light: Sci. Appl.* **2019**, *8*, 88.
[36] W. Liu, Y. Wu, C.-K. Duan, X. Rong, J. Du, *Phys. Rev. Lett.* **2021**, *126*, 170506.

[37] M. Abbasi, W. Chen, M. Naghiloo, Y. N. Joglekar, K. W. Murch, *Phys. Rev. Lett.* **2022**, *128*, 160401.
[38] H. Nasari, G. Lopez-Galmiche, H. E. Lopez-Aviles, A. Schumer, A. U. Hassan, Q.i Zhong, S. Rotter, P. Likamwa, D. N. Christodoulides, M. Khajavikhan, *Nature* **2022**, *605*, 256.
[39] E.-M. Graefe, A. A. Mailybaev, N. Moiseyev, *Phys. Rev. A* **2013**, *88*, 033842.
[40] X.-L. Zhang, S. Wang, B. Hou, C. T. Chan, *Phys. Rev. X* **2018**, *8*, 021066.
[41] I. I. Arkhipov, A. Miranowicz, F. Minganti, S. K. Özdemir, F. Nori, *Nat. Commun.* **2023**, *14*, 2076.
[42] H. Hodaei, M.-A. Miri, M. Heinrich, D. N. Christodoulides, M. Khajavikhan, *Science* **2014**, *346*, 975.
[43] L. Feng, Z.i J. Wong, R.-M. Ma, Y. Wang, X. Zhang, *Science* **2014**, *346*, 972.
[44] A. Schumer, Y. G. N. Liu, J. Leshin, L. Ding, Y. Alahmadi, A. U. Hassan, H. Nasari, S. Rotter, D. N. Christodoulides, P. Likamwa, M. Khajavikhan, *Science* **2022**, *375*, 884.
[45] H. Hodaei, A. U. Hassan, S. Wittek, H. Garcia-Gracia, R. El-Ganainy, D. N. Christodoulides, M. Khajavikhan, *Nature* **2017**, *548*, 187.
[46] W. Chen, S. Kaya Özdemir, G. Zhao, J. Wiersig, L. Yang, *Nature* **2017**, *548*, 192.
[47] P.-Y. Chen, M. Sakhdari, M. Hajizadegan, Q. Cui, M. M.-C. Cheng, R. El-Ganainy, A. Alù, *Nat. Electron.* **2018**, *1*, 297.
[48] Z. Dong, Z. Li, F. Yang, C.-W. Qiu, J. S. Ho, *Nat. Electron.* **2019**, *2*, 335.
[49] M. P. Hokmabadi, A. Schumer, D. N. Christodoulides, M. Khajavikhan, *Nature* **2019**, *576*, 70.
[50] J.-H. Park, A. Ndao, W. Cai, L. Hsu, A. Kodigala, T. Lepetit, Y.u-H. Lo, B. Kanté, *Nat. Phys.* **2020**, *16*, 462.
[51] J. Wiersig, *Phys. Rev. Lett.* **2014**, *112*, 203901.
[52] R. Kononchuk, T. Kottos, *Phys. Rev. Res.* **2020**, *2*, 023252.
[53] Z. Xiao, H. Li, T. Kottos, A. Alù, *Phys. Rev. Lett.* **2019**, *123*, 213901.
[54] M. Zhang, W. Sweeney, C. W. Hsu, L. Yang, A. ? D. Stone, L. Jiang, *Phys. Rev. Lett.* **2019**, *123*, 180501.
[55] H.-K. Lau, A. A. Clerk, *Nat. Commun.* **2018**, *9*, 4320.
[56] J. Wiersig, *Nat. Commun.* **2020**, *11*, 2454.
[57] Y.u-H. Lai, Y.u-K. Lu, M.-G. Suh, Z. Yuan, K. Vahala, *Nature* **2019**, *576*, 65.
[58] H. Wang, Y.u-H. Lai, Z. Yuan, M.-G. Suh, K. Vahala, *Nat. Commun.* **2020**, *11*, 1610.
[59] W. Langbein, *Phys. Rev. A* **2018**, *98*, 023805.
[60] J. Wiersig, *Phys. Rev. A* **2020**, *101*, 053846.
[61] A. Guo, G. J. Salamo, D. Duchesne, R. Morandotti, M. Volatier-Ravat, V. Aimez, G. A. Siviloglou, D. N. Christodoulides, *Phys. Rev. Lett.* **2009**, *103*, 093902.
[62] C. Wang, X. Jiang, G. Zhao, M. Zhang, C. W. Hsu, B.o Peng, A. D. Stone, L. Jiang, L. Yang, *Nat. Phys.* **2020**, *16*, 334.
[63] Z. Lin, H. Ramezani, T. Eichelkraut, T. Kottos, H. Cao, D. N. Christodoulides, *Phys. Rev. Lett.* **2011**, *106*, 213901.
[64] B.o Zhen, C. W. Hsu, Y. Igarashi, L. Lu, I. Kaminer, A. Pick, S.-L. Chua, J. D. Joannopoulos, M. Soljacic, *Nature* **2015**, *525*, 354.
[65] H.-Z. Chen, T. Liu, H.-Y.i Luan, R.-J. Liu, X.-Y. Wang, X.-F. Zhu, Y.-B.o Li, Z.-M. Gu, S.-J. Liang, H.e Gao, L. Lu, L.i Ge, S. Zhang, J. Zhu, R.-M. Ma, *Nat. Phys.* **2020**, *16*, 571.
[66] B.o Wang, Z. Tang, T. Chen, X. Zhang, *Laser Photonics Rev.* **2022**, *16*, 2100519.
[67] R. Kononchuk, J. Cai, F. Ellis, R. Thevamaran, T. Kottos, *Nature* **2022**, *607*, 697.
[68] Y.u-L. Fang, J.-L. Zhao, Y.u Zhang, D.-X.u Chen, Q.i-C. Wu, Y.-H. Zhou, C.-P. Yang, F. Nori, *Commun. Phys.* **2021**, *4*, 223.
[69] F. Minganti, A. Miranowicz, R. W. Chhajlany, F. Nori, *Phys. Rev. A* **2019**, *100*, 062131.
[70] I. I. Arkhipov, A. Miranowicz, F. Minganti, F. Nori, *Phys. Rev. A* **2020**, *101*, 013812.
[71] I. I. Arkhipov, A. Miranowicz, F. Minganti, F. Nori, *Phys. Rev. A* **2019**, *102*, 033715.
[72] R. Horodecki, P. Horodecki, M. Horodecki, K. Horodecki, *Rev. Mod. Phys.* **2009**, *81*, 865.
[73] T. D. Ladd, F. Jelezko, R. Laflamme, Y. Nakamura, C. Monroe, J. L. O'brien, *Nature* **2010**, *464*, 45.
[74] J.-W. Pan, Z.-B. Chen, C.-Y. Lu, H. Weinfurter, A. Zeilinger, M. Zukowski, *Rev. Mod. Phys.* **2012**, *84*, 777.
[75] Q.i-P. Su, Y.u Zhang, L.i Yu, J.-Q.i Zhou, J.-S. Jin, X.-Q. Xu, S.-J. Xiong, Q. Xu, Z. Sun, K. Chen, F. Nori, C.-P. Yang, *npj Quantum Inf.* **2019**, *5*, 40.
[76] Z. Yan, Y. R. Zhang, M. Gong, Y. Wu, Y. Zheng, S. Li, C. Wang, F. Liang, J. Lin, Y. Xu, C. Guo, L. Sun, C. Z. Peng, K. Xia, H. Deng, H. Rong, J. Q. You, F. Nori, H. Fan, X. Zhu, J. W. Pan, *Science* **2019**, *364*, 753.
[77] W. D. Heiss, *Eur. Phys. J. D* **1999**, *7*, 1.
[78] C. Dembowski, B. Dietz, H.-D. Gräf, H. L. Harney, A. Heine, W. D. Heiss, A. Richter, *Phys. Rev. E* **2004**, *69*, 056216.
[79] B. Dietz, H. L. Harney, O. N. Kirillov, M. Miski-Oglu, A. Richter, F. Schäfer, *Phys. Rev. Lett.* **2011**, *106*, 150403.
[80] S. Bittner, B. Dietz, U. Günther, H. L. Harney, M. MiskiOglu, A. Richter, F. Schäfer, *Phys. Rev. Lett.* **2012**, *108*, 024101.
[81] J. L. O'brien, G. J. Pryde, A. G. White, T. C. Ralph, D. Branning, *Nature* **2003**, *426*, 264.
[82] R. Okamoto, H. F. Hofmann, S. Takeuchi, K. Sasaki, *Phys. Rev. Lett.* **2005**, *95*, 210506.